ADVANCED FUNCTIONAL MATERIALS
www.afm-journal.de

Solution-Processed Nickel Oxide Hole Transport Layers in High Efficiency Polymer Photovoltaic Cells

Jesse R. Manders, Sai-Wing Tsang, Michael J. Hartel, Tzung-Han Lai, Song Chen, Chad M. Amb, John R. Reynolds,* and Franky So**

The detailed characterization of solution-derived nickel (II) oxide (NiO) hole-transporting layer (HTL) films and their application in high efficiency organic photovoltaic (OPV) cells is reported. The NiO precursor solution is examined in situ to determine the chemical species present. Coordination complexes of monoethanolamine (MEA) with Ni in ethanol thermally decompose to form non-stoichiometric NiO. Specifically, the $[Ni(MEA)_2(OAc)]^+$ ion is found to be the most prevalent species in the precursor solution. The defect-induced Ni^{3+} ion, which is present in non-stoichiometric NiO and signifies the p-type conduction of NiO, as well as the dipolar nickel oxyhydroxide (NiOOH) species are confirmed using X-ray photoelectron spectroscopy. Bulk heterojunction (BHJ) solar cells with a polymer/fullerene photoactive layer blend composed of poly-dithienogermole-thienopyrrolodione (pDTG-TPD) and [6,6]-phenyl-C71-butyric acid methyl ester ($PC_{71}BM$) are fabricated using these solution-processed NiO films. The resulting devices show an average power conversion efficiency (PCE) of 7.8%, which is a 15% improvement over devices utilizing a poly(3,4-ethylenedioxythiophene):poly(styrenesulfonate) (PEDOT:PSS) HTL. The enhancement is due to the optical resonance in the solar cell and the hydrophobicity of NiO, which promotes a more homogeneous donor/acceptor morphology in the active layer at the NiO/BHJ interface. Finally, devices incorporating NiO as a HTL are more stable in air than devices using PEDOT:PSS.

1. Introduction

In a society concerned with environmental, economic, and geopolitical consequences of energy consumption, new alternatives to traditional energy sources are needed. With rapid progress being made in organic photovoltaics, they are becoming a viable source of renewable energy, as power conversion efficiencies (PCEs) exceeding 8% have been demonstrated.[1,2] Traditional bulk heterojunction polymer solar cells consist of a transparent indium tin oxide (ITO) anode, a hole transport layer, a photoactive layer, and a top cathode. Hole transport layers must have high optical transparency, good chemical stability, a large ionization potential, and good electron blocking capability.

In a typical polymer solar cell, poly(3,4-ethylenedioxythiophene):poly(styrenesulfonate) (PEDOT:PSS) is used as the hole-transporting layer (HTL) and has a work function (Φ) of 5.2 eV. However, its acidity, tendency to absorb water, and inability to block electrons effectively are factors which contribute to device performance problems and degradation.[3] Nickel oxide is emerging as an alternative HTL for polymer solar cells.[4–14] Pure, stoichiometric NiO is an excellent insulator, with room temperature conductivity on the order of 10^{-13} S cm^{-1},[15] while non-stoichiometric NiO is a wide bandgap p-type semiconductor.[16–21] The p-type conductivity of NiO originates from two positively charged holes which accompany each Ni^{2+} vacancy in the lattice for charge neutrality.[16,22,23] These holes are quasi-localized on Ni^{2+} ions near the vacancy in the lattice, generating two Ni^{3+} ions for each Ni^{2+} vacancy.[16,24] The valence band edge of NiO is well-aligned to the highest occupied molecular orbital (HOMO) levels of many p-type conjugated polymers for photovoltaics.[12,21]

Irwin et al. first demonstrated an enhancement in polymer solar cell performance with a NiO electron blocking layer deposited via pulsed laser deposition.[12,25] Recently, solution-processed NiO was also reported for polymer photovoltaics.[13,14,21] A nickel ink made from nickel formate and ethylenediamine was used as the precursor in those reports. Here, we chose nickel acetate tetrahydrate and monoethanolamine precursors in an ethanolic solution, as this presents a set of materials not yet

J. R. Manders, Dr. S.-W. Tsang, M. J. Hartel, T.-H. Lai, S. Chen, Prof. F. So
Department of Materials Science and Engineering
University of Florida
Gainesville, FL 32611 USA
E-mail: fso@mse.ufl.edu

Dr. C. M. Amb
The George and Josephine Butler Polymer Research Laboratory
Department of Chemistry
Center for Macromolecular Science and Engineering
University of Florida
Gainesville, FL 32611 USA
E-mail: chad.amb@hotmail.com

Prof. J. R. Reynolds
School of Chemistry and Biochemistry
School of Materials Science and Engineering
Center for Organic Photonics and Electronics
Georgia Institute of Technology
Atlanta, GA 30332-0400 USA
E-mail:r eynolds@chemistry.gatech.edu

DOI:10. 1002/adfm.201202269

© 2013 WILEY-VCH Verlag GmbH & Co. KGaA, Weinheim

used to create NiO in solar cells. Using these NiO solution precursors, we investigated the chemical, optical, electronic, and structural properties of solution-processed NiO from conception of the precursors to their impact on the solar cell.

Combining this solution-derived NiO with our low bandgap polymer poly-dithienogermole-thienopyrrolodione (pDTG-TPD),[1,26] we fabricated solar cells with an average power conversion efficiency (PCE) of 7.8%. This is a 15% enhancement over reference devices with PEDOT:PSS as the HTL. Contrary to previous reports,[4,5,12–14,21] we found that neither the effective work function difference between NiO and PEDOT:PSS nor the manifestation of the better electron blocking ability of NiO in the reverse saturation current were the most important factors in the device improvement. Rather, this solution-derived NiO provided a more favorable surface to form optimized donor/acceptor nanoscale phase morphology at the HTL/bulk heterojunction (BHJ) interface, reducing the series resistance and increasing the shunt resistance in the device. Additionally, optical absorption in the solar cells is improved due to an optical resonance shift when NiO is substituted for PEDOT:PSS. Finally, the devices with NiO were found to be more air-stable than devices with PEDOT:PSS under ambient conditions.

2. Results and Discussion

2.1. NiO Precursor Composition

The precursors used to synthesize common solution-derived metal oxides consist of a solution of a metal salt and an amine compound in an alcohol solvent. The amine compounds for metal oxide synthesis are often considered to be a sol modifier or stabilizer.[27–29] In contrast to these suggestions, we found that the amine plays an active role in the precursor solution, forming ionic complexes with the metal, in agreement with previous studies,[30] rather than a passive stabilizer role.

To synthesize the precursor solution, we dissolved nickel acetate tetrahydrate ($Ni(OAc)_2 \cdot 4H_2O$) and monoethanolamine (MEA) in ethanol. To determine the exact role MEA plays in the reaction, high-resolution electrospray ionization mass spectrometry (ESI-MS) was used to sample the ionic species in the solution. The main species found in the precursor solution was the $[Ni(MEA)_2(OAc)]^+$ ion which has a mass-to-charge ratio (m/z) of 239.0520. The composition of this ion was confirmed by comparing the experimental data to the theoretical mass-to-charge ratio (see Supporting Information Figure S1,S2). From these data, we conclude that MEA acts as a ligand that coordinates to nickel to form ionic complexes and plays a larger role than a solution stabilizer. Therefore, the formation of NiO requires complete thermolysis of the ionic complexes, the details of which will be presented in the following section.

2.2. Characterization of NiO films

2.2.1. Optical Properties

Figure 1a shows the UV-vis-NIR absorption spectra of the precursor solution and the NiO films fabricated at different temperatures. Nickel oxide films were formed by thermally decomposing spin-cast films of the precursor solution in air. The absorption spectrum of the precursor solution is consistent with the typical d-d transitions of octahedral nickel complexes coordinated mostly by oxygen donor atoms. When spin-cast precursor films were heated to 230 °C, the absorption corresponding to the precursor remained in the spectrum while a strong absorption beginning at 330 nm emerged, corresponding to the bandgap edge of NiO. These results indicate that the precursor was not completely converted to NiO at 230 °C. When the films were heated to 275 °C, the precursor was completely converted into NiO, as shown by the strong band-edge absorption

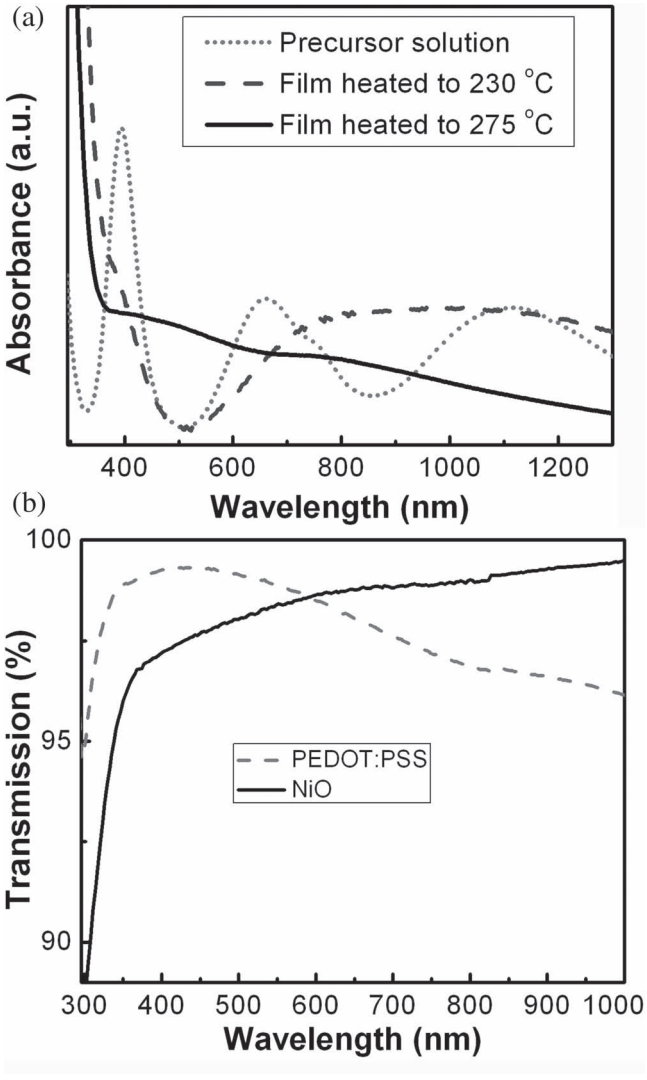

Figure 1. a) Absorption spectra of the transformation of the precursor into NiO. The material transforms from the precursor to a full nickel oxide film by thermal decomposition of the precursor materials, as is shown by the elimination of the visible and IR absorption peaks, and the appearance of the UV band-edge of NiO. b) Transmission spectrum of 5 nm thin NiO films is compared to 30 nm thin PEDOT:PSS films used in the optimized solar cells. The thin NiO films are more transparent than the PEDOT:PSS films used in solar cells at wavelengths longer than 590 nm.

© 2013 WILEY-VCH Verlag GmbH & Co. KGaA, Weinheim

at 330 nm and the absence of precursor absorption. The broad absorption tail at energies below the bandgap for NiO fabricated at 275 °C is caused by nickel vacancies, resulting in a slight coloration in the films.[31,32] This coloration in thin films does not significantly hinder the optical transparency, which is important for solar cell performance.

Figure 1b shows the optical transmission spectrum of a 5 nm thick solution-derived NiO film, along with the spectrum for a 30 nm thick PEDOT:PSS film used as a reference. These were the thicknesses of the HTL films that gave optimized performance in the solar cells discussed later. The NiO film is more than 95% transparent across the entire visible and NIR spectra. At wavelengths longer than 590 nm, where the solar flux is largest, the NiO film is more transparent than the PEDOT:PSS film, which is desirable for solar cell applications. These results suggest that NiO is a promising candidate for HTL in OPV cells.

2.2.2. Electronic Structure and Composition of NiO Films

To understand the composition of the solution-derived NiO films fabricated at 275 °C, the films were studied by X-ray photoelectron spectroscopy (XPS). **Figure 2**a shows the XPS spectrum for the Ni $2p_{3/2}$ state, which can be separated into three peaks. First, the peak centered at a binding energy of 853.7 eV corresponds to Ni^{2+} in the standard Ni-O octahedral bonding configuration in cubic rocksalt NiO.[33–35] Second, the broad peak centered at 860.8 eV has been ascribed to a shake-up process in the NiO structure.[34] Finally, the peak centered at 855.5 eV has been ascribed to the Ni^{2+} vacancy-induced Ni^{3+} ion[33,34,36] or nickel hydroxides and oxyhydroxides.[34,37–41]

Figure 2b shows the XPS spectrum for the O 1s state, which can be separated into two distinct peaks. The peak centered at 529.2 eV confirms the Ni-O octahedral bonding in NiO.[34] The peak at 531.0 eV is indicative of nickel hydroxides and oxyhydroxides, including defective nickel oxide with hydroxyl groups adsorbed on the surface.[40–42] However, this peak has also been assigned to oxygen interactions with a nickel-deficient lattice, suggesting some correlation with nickel vacancy concentration.[34,36]

Because there are several possible sources of the XPS signals at 855.5 eV and 531.0 eV, we further characterized the structural and chemical features of the film by grazing-incidence X-ray diffraction (GIXRD) and angle-resolved XPS to examine which of these sources are present, if not all of them. Detailed analysis of the NiO films by GIXRD showed the typical NiO diffraction pattern with small grains approximately 1 nm in diameter, as estimated from the Scherrer equation.[43] The presence of nickel vacancies is consistent with shifted diffraction peaks relative to those of stoichiometric NiO (see Supporting Information Figure S3). Angle-resolved XPS spectra of the O 1s and Ni $2p_{3/2}$ regions show an increased intensity of the 855.5 eV and 531.0 eV peaks at a lower take-off angle due to the presence of hydroxides and oxyhydroxides at the extreme surface layers caused by air exposure (see Supporting Information Figure S4). The NiOOH species, in particular, was found to be an essential surface dipolar feature for favorable contacts in bulk heterojunction PV cells.[41] Additionally, as discussed above, the NiO films do have a pale black tinge, which further confirms the vacancy-induced Ni^{3+} and NiOOH.[31,32,44]

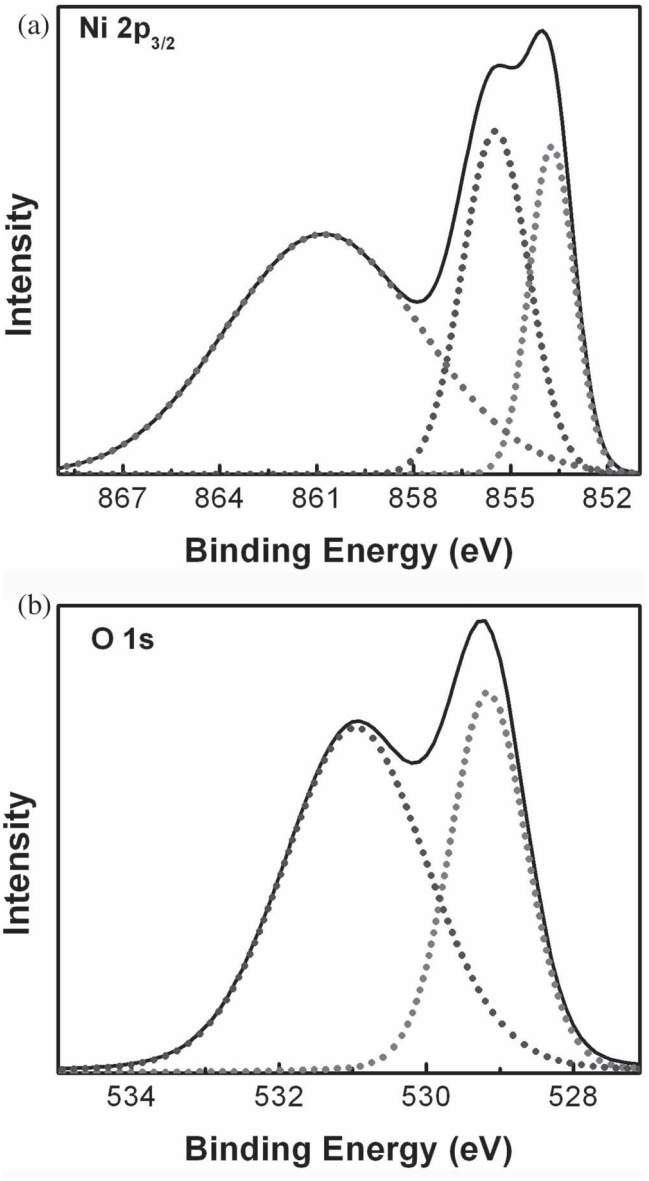

Figure 2. a) High resolution Ni $2p_{3/2}$ XPS acquisition for NiO. The spectrum shows three contributions: one from Ni^{2+} in the octahedral NiO configuration at low binding energy, one from hydroxylated or defective NiO at an intermediate binding energy, and one from a shake-up process in the NiO lattice at the highest binding energy. b) High resolution O 1s XPS acquisition for NiO. The spectrum shows two contributions: one from O^{2-} in the octahedral NiO configuration at low binding energy and one from hydroxylated or defective NiO at a higher binding energy.

2.3. Photovoltaic Cells with Solution-Processed Nickel Oxide

Using the NiO films described above as a hole transporting layer, we fabricated BHJ solar cells based on the high efficiency pDTG-TPD:$PC_{71}BM$ photoactive layer. The device structure and the energy band diagram of the NiO device are shown in **Figure 3**a along with that of the reference PEDOT:PSS device.[26,45,46] The device fabrication details are reported in the Experimental Section.

© 2013 WILEY-VCH Verlag GmbH & Co. KGaA, Weinheim

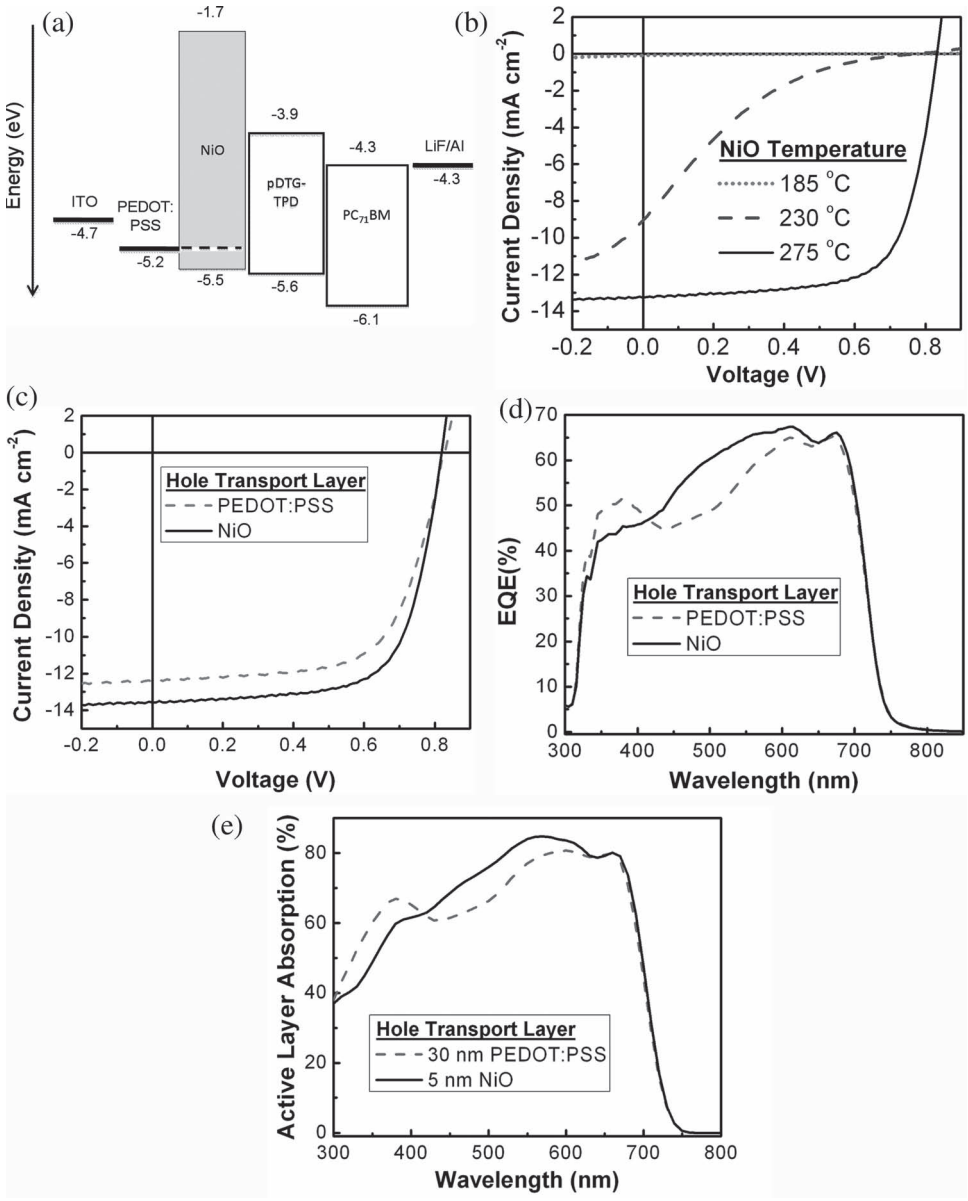

Figure 3. a) Device structure and energy levels with respect to vacuum of the materials used in the photovoltaic cells. b) Illuminated *J–V* characteristics of the solar cells with NiO fabricated at different temperatures. After the full formation of NiO at 275 °C the solar cells perform optimally, with a PCE of 7.8%. c) Illuminated *J–V* characteristics of solar cells comprising NiO or PEDOT:PSS HTLs. The solar cells with NiO as the HTL outperform those with PEDOT:PSS due to a higher fill factor and short circuit current. d) External quantum efficiency of solar cells fabricated in this study. The EQE of solar cells with NiO is greater at nearly all wavelengths of incident light. The spectrum shift between the device is caused by optical resonance changes within the solar cell. e) Simulated spectral absorption for solar cells with NiO or PEDOT:PSS HTLs. The spectra are in close agreement with the experimental spectra, indicating that the shift is due to optical resonance in the solar cells.

2.3.1. Solar Cell Characteristics

To demonstrate the viability of these NiO films for photovoltaic applications, we fabricated solar cells with NiO as the HTL with three different NiO precursor processing temperatures: below the completed precursor thermolysis at 185 °C, in the middle of thermolysis at 230 °C, and after complete thermolysis of the NiO precursor films at 275 °C. The current density–voltage (*J–V*) characteristics of these solar cells are presented in Figure 3b with the performance characteristics summarized in **Table 1**. At a processing temperature of 185 °C, the precursor

Table 1. Performance of solar cells fabricated at various NiO processing temperatures. One standard deviation is reported in parenthesis. The device with NiO fabricated at 275 °C is the optimized device due to full conversion from precursor to NiO.

NiO Temperature	V_{oc} [V]	J_{sc} [mA cm^{-2}]	FF [%]	PCE [%]
185 °C	0.60	0.09 (0.01)	13.0 (0.1)	0.007 (0.001)
230 °C	0.76	6.4 (1.9)	12.1 (0.8)	0.61 (0.2)
275 °C	0.82	13.9 (0.3)	68.4 (0.4)	7.82 (0.2)

© 2013 WILEY-VCH Verlag GmbH & Co. KGaA, Weinheim

Table 2. Device characteristics of the solar cells fabricated in this study. One standard deviation is reported in parenthesis. Series resistance was calculated using the illuminated *J–V* values converging to V_{oc}. Shunt resistance was calculated using illuminated *J–V* values converging to J_{sc}.

HTL	V_{oc} [V]	J_{sc} [mA cm^{-2}]	*FF* [%]	PCE [%]	R_s [Ωc m^2]	R_{sh} [Ωc m^2]	V_{bi} [EA]
PEDOT:PSS	0.83 (0.005)	12.7 (0.2)	64.2 (0.3)	6.8 (0.1)	13.1 (1.1)	348.4 (90.4)	0.96 V
5 nm NiO	0.82 (0.006)	13.9 (0.3)	68.4 (0.4)	7.8 (0.2)	7.9 (1.3)	455.4 (72.5)	0.95 V

did not significantly decompose into NiO, resulting in a non-conductive HTL and poor solar cell performance, as expected. At 230 °C, the HTL film contained a mixture of residual non-conductive precursor and NiO, and thus the solar cell showed an improvement in short circuit current density (J_{sc}) and open circuit voltage (V_{oc}). When heated to 275 °C, the film fully converted to NiO and the solar cell showed optimum performance with an average PCE of 7.8%. We note that in contrast to previous reports of solution-processed NiO in PV cells, where oxygen plasma treatment of NiO is needed for optimized devices,[13,14,21] the NiO films used here did not require any post-deposition surface treatment for optimized performance. In fact, all of the solar cell performance parameters decreased when UV-O_3 treatment was applied to NiO before depositing the active layer (see Supporting Information Figure S5).

We benchmarked the performance of our NiO-based devices by fabricating them side-by-side with PEDOT:PSS-based devices. The *J–V* characteristics of the solar cells with either an optimized 5 nm thin NiO HTL or an optimized reference 30 nm thin PEDOT:PSS film are shown in Figure 3c. The performance characteristics are summarized in **Table 2**. The open circuit voltages of the devices with PEDOT:PSS were 10 mV higher than those with NiO. Devices with PEDOT:PSS produced an average J_{sc} of 12.7 mA cm^{-2}, while those with NiO produced an average of 13.9 mA cm^{-2}, a 9.4% ± 2.9% improvement. The average fill factor (*FF*) for devices with PEDOT:PSS was 64.2%, while for those with NiO it increased to 68.4%, a 6.5% ± 0.8% improvement. Because of the enhanced J_{sc} and *FF*, devices with NiO showed significantly higher PCEs than those with PEDOT:PSS. The optimized PEDOT:PSS-based device showed an average PCE of 6.8% while the optimized NiO devices showed an average PCE of 7.8%, a 14.7% ± 0.1% improvement. To understand why the solar cells performed as such relative to each other, we studied their performance parameters in more detail.

2.3.2. Analysis of the Solar Cell Performance

In previous work with solution-processed NiO, the V_{oc} of the NiO devices was higher than that of the PEDOT:PSS devices due to the larger work function of NiO and increase in electron blocking capability, i.e., lower dark reverse saturation current (J_o).[13,21,41] In the limit of large shunt resistance, which is applicable here and is discussed later, the relationship between V_{oc} and J_o described in the ideal diode model[21] can be written as:

$$V_{oc} \approx \frac{nkT}{q} \ln\left(1 + \frac{J_{sc}}{J_o}\right) \quad (1)$$

where n is the diode ideality factor, k is Boltzmann's constant, T is the absolute temperature, and q is the magnitude of the elementary charge. Our device data showed that devices with NiO have a lower J_o than the devices with PEDOT:PSS. This suggests that there is improved electron blocking in the NiO devices. Based on Equation (1), a lower J_o should also lead to a higher V_{oc}, which is not the case here. Furthermore, the magnitude of the predicted V_{oc} in these devices does not agree with this relation when we insert the measured values for the J_{sc}, J_o, and n into Equation (1). Fitting the dark current data yields a diode ideality factor in both devices of 1.27 (see Supporting Information Figure S6). As an example, we calculated the expected V_{oc} using the J_o values at –0.5 V: J_o for PEDOT:PSS devices is 2.5×10^{-5} mA/cm^2, while for NiO devices it is 1.7×10^{-5} mA/cm^2. The result is a calculated V_{oc} for the PEDOT:PSS devices of 0.44 V, while for the NiO devices it is slightly higher at 0.46 V. Clearly, this is not in agreement with the experimental data, either in magnitude, or in that PEDOT:PSS-based devices have a larger V_{oc}, experimentally. Furthermore, our results indicate that the ideal diode equation is unable to fully account for the device behavior, suggesting the behavior of the solar cells is more complicated than this simple model. To fully explain the difference in V_{oc} and ascertain the source of the enhanced short circuit current density and fill factor in our devices, we measured the built-in voltage (V_{bi}) of the solar cells with electroabsorption (EA), studied the spectral response of the solar cells and the morphology of the active layer at the HTL/active layer interface.

The built-in voltage of solar cells is the difference in the effective work functions of the cathode and anode/HTL. Using EA, we determined that the built-in voltage in the NiO and PEDOT:PSS devices was 0.95 V, and 0.96 V, respectively (see Supporting Information Figure S7). Thus, if we take the work function of PEDOT:PSS to be 5.20 eV, as stated above, then the effective work function of the NiO in the device is 5.19 eV, as extracted from the EA data. This 10 mV difference in the V_{bi} is the same as the 10 mV difference in the V_{oc} of the two solar cells. It is reasonable to conclude that changing the work function of the HTL plays a role in controlling the V_{oc} in this system since the HOMO level of pDTG-TPD lies below the Fermi level of NiO that has been fabricated outside of vacuum conditions.[26,47] Similar modulation of the V_{oc} by modification of the HTL work function was realized with PCDTBT-based solar cells, where PCDTBT also has a deep HOMO level.[21] However, in cases where P3HT was used as the donor polymer in the BHJ, no further modulation of the V_{oc} was observed when increasing the work function of the HTL. This was because the HOMO level of P3HT lay closer to the vacuum level than the Fermi level of the HTL.[14,21,48] That is, modulating the V_{oc} by changing HTL work function seemed to occur only when the HOMO of the donor polymer lies below the Fermi level of the HTL. Based on these results, we conclude that the V_{oc} is controlled by the

© 2013 WILEY-VCH Verlag GmbH & Co. KGaA, Weinheim

work function of the HTL in this system since the Fermi level of both HTLs lies above the HOMO level of the donor polymer, and that the enhancements in J_{sc} and fill factor in the NiO cells are not due to the difference in work function of the HTLs. To determine the cause of increased J_{sc}, we examined the external quantum efficiency (EQE) and optical resonance in the devices.

The EQEs for both devices are shown in Figure 3d. The global maximum EQE is in the NiO device and has a value of 67% at 615 nm, which is in agreement with the slightly higher optical transmission of NiO in this wavelength range. The maximum EQE for PEDOT:PSS-based devices is slightly lower, with a value of 65% at 610 nm. Interestingly, while the transmission of NiO is slightly lower than that of PEDOT:PSS at wavelengths between 425–590 nm, the EQE in the NiO devices is actually higher. This enhancement in the EQE is due to the different refractive indices of the HTLs and optical resonance in the devices and is one of the main reasons for the enhancement in J_{sc} in the NiO devices. The optical resonance change has been confirmed by our finite-difference time-domain (FDTD) method optical modeling results, as shown in Figure 3e.

Since the NiO work function and electron blocking ability's manifestation in J_o are not the primary reasons for the enhancement in overall device PCE, and the fill factor improvement is not directly correlated with the optical resonance shift, we studied the differences in surface morphology and surface energy between NiO and PEDOT:PSS. Based on the atomic force microscopy (AFM) results, the root-mean-square (RMS) roughness values for PEDOT:PSS and NiO were found to be 0.79 nm and 0.88 nm, respectively. This small difference in roughness should not affect the solar cell performance. In previous work by Hau et al., changes in the morphology of the active layer in inverted solar cells were correlated with changes of surface energy of the TiO_2 or ZnO electron transport layers (ETLs) on which the active layer was deposited.[49,50] Depositing various self-assembled monolayers on the ETLs prior to depositing the active layer modified the surface energy of the ETLs. These active layer morphology changes yielded an increase in short circuit current and fill factor in the solar cells.[49,50] This type of analysis has not been performed to explain the performance of solar cells with NiO as a HTL. We examined the surface energy of the HTLs by measuring water contact angles

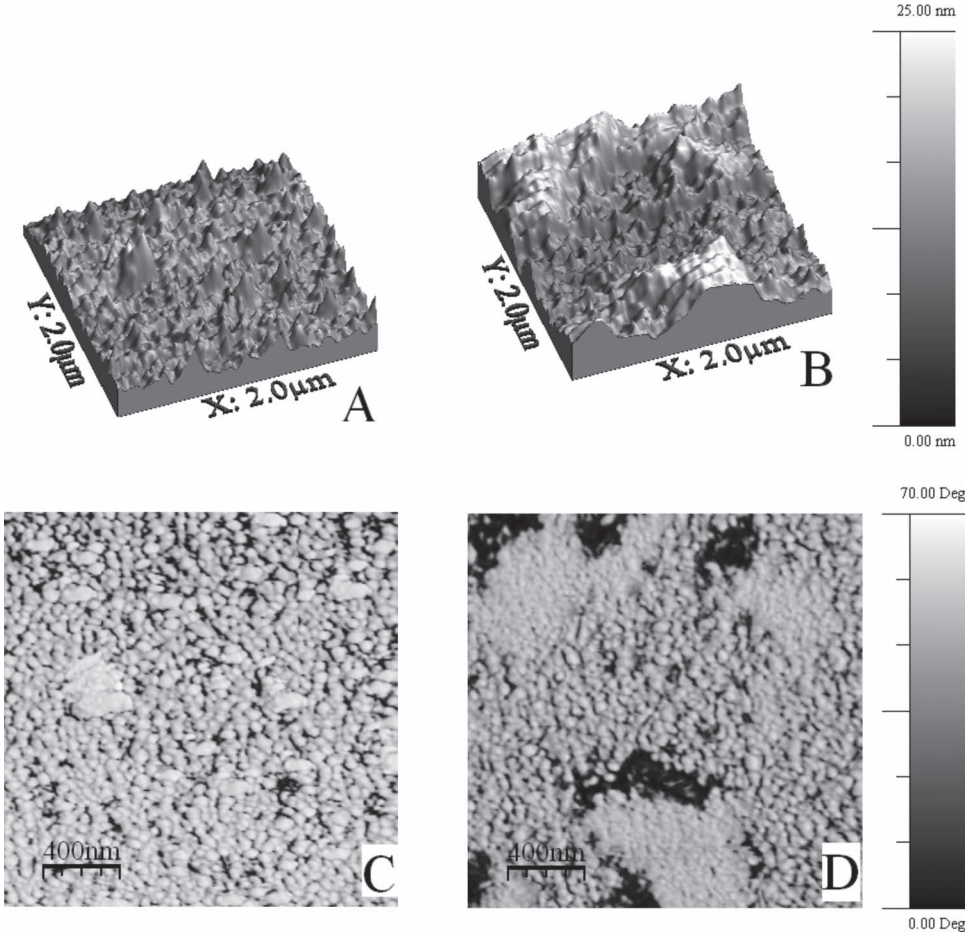

Figure 4. AFM roughness images of 10 nm thick BHJ films on a) NiO and b) PEDOT:PSS showing the contrast in physical formation of the films on different HTLs. The active layer films deposited on NiO are smoother than those deposited on PEDOT:PSS. AFM phase images of thin polymer/fullerene blend layers on c) NiO and d) PEDOT:PSS, showing a drastic change in material distribution near the HTL/active layer interface, caused by surface energy differences of NiO and PEDOT:PSS. The scale bar is 400 nm and the scan area is 2 μm × 2 μm.[52]

© 2013 WILEY-VCH Verlag GmbH & Co. KGaA, Weinheim

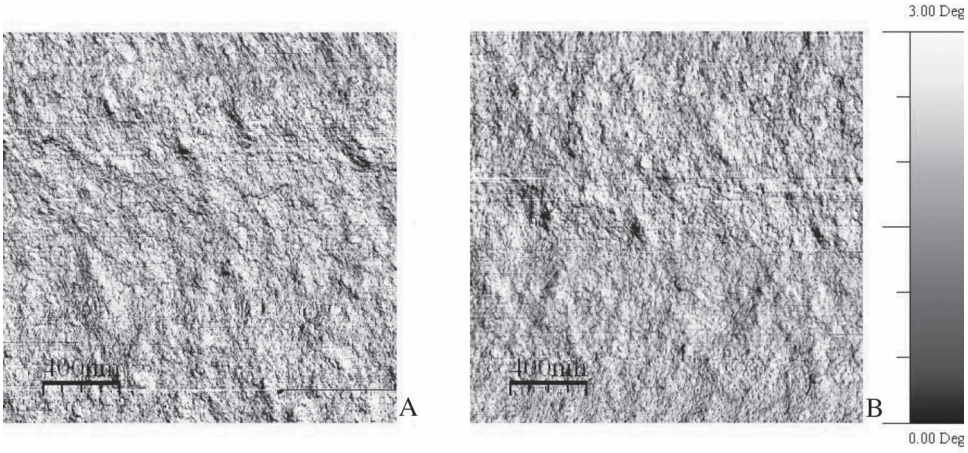

Figure 5. AFM phase images of the full ≈100 nm thick BHJ films on a) NiO and b) PEDOT:PSS. The images show a similar lateral phase distribution for both types of films. The scale bar is 400 nm and the scan area is 2 μm × 2 μm.

of the NiO and PEDOT:PSS films. The average contact angles were 29.3° ± 2.8° for NiO and 12.5° ± 1.4° for PEDOT:PSS. These results indicate that the NiO surface is less hydrophilic than PEDOT:PSS, allowing better wetting by nonpolar solvents such as that used for the pDTG-TPD/$PC_{71}BM$ active layer. This improved wetting leads to improved active layer film formation and possibly donor/acceptor phase morphology, as observed in previous work described above. To confirm the improvement in donor/acceptor phase morphology near the HTL/active layer interface, we deposited a 10 nm thick active layer film on both PEDOT:PSS and NiO surfaces. **Figure 4**a,b show the AFM roughness results. The RMS roughness of the thin active layer film on NiO was 2.3 nm, while the roughness of the film on PEDOT:PSS was 3.6 nm. This indicates that the film formation and physical contact at the interface of the active layer and the HTL is more uniform when using NiO. To further examine the chemical differences at the interface, we examined the phase distribution of these thin BHJ films. As shown in Figure 4c,d, the active layer film deposited on NiO has a more homogeneous lateral donor/acceptor phase distribution near HTL/active layer interface than the film deposited on PEDOT:PSS. This improved phase morphology should lead to a more uniform electrical contact to NiO. In fact, there is a 40% lower series resistance (R_s) and 31% higher shunt resistance (R_{sh}) in the NiO devices compared to the PEDOT:PSS devices as shown in Table 2. The decrease in series resistance indicates that holes are extracted more efficiently, while the increase in shunt resistance suggests that there is less interfacial recombination in the NiO device and that NiO is blocking electrons more effectively.

It is possible that both the energy band alignment of NiO with the BHJ HOMO-lowest unoccupied molecular orbital (LUMO) levels and the improved donor/acceptor phase morphology are both contributing to the change in parasitic resistances in these devices. In this case, the NiO is actually mitigating the parasitic resistances and improving fill factor due to improved donor/acceptor phase morphology at the NiO/BHJ interface and improved contact. This is where the electron blocking ability of NiO is expected to have its most pronounced effect.

Additionally, we found that there is a change in the lateral donor/acceptor phase distribution as a function of distance from the HTL/BHJ interface. An inspection of the full ≈100 nm thick BHJ layer by AFM revealed a very similar donor/acceptor phase distribution between films deposited either on NiO or PEDOT:PSS, as shown in **Figure 5**. The RMS roughness of both BHJ films is approximately 3.1 nm. This suggests that the lateral donor/acceptor phase morphology is strongly affected by the HTL surface energy at the HTL/BHJ interface, while it is weakly, if at all, affected far away from the interface. A detailed study of the vertical donor/acceptor phase separation is beyond the scope of this work, but would help elucidate the exact interfacial science present here. Here, we conclude that this improved donor/acceptor phase morphology at the HTL/BHJ interface and enhanced optical absorption in the device are the major factors in the success of the NiO device.

2.3.3. Stability of Solar Cells

The final indicator of the viability of NiO in solar cells is the device storage stability. We performed a side-by-side comparison of unencapsulated NiO- and PEDOT:PSS-based devices stored in the laboratory's ambient conditions. As shown in **Figure 6**, the NiO-based devices degraded much slower than the PEDOT:PSS devices. This is in agreement with previous work on degradation of solar cells with NiO compared to PEDOT:PSS.[5,21] Most of the difference in performance loss between the two devices was due to the decrease in J_{sc}, indicating the difference in device degradation is due to HTL and/or interfacial degradation. Indeed, previous studies have shown that the acidity and hygroscopic nature of PEDOT:PSS corrodes the ITO electrode and PEDOT:PSS itself;[3] both are problems for organic photovoltaics at this time which can be overcome by substituting a more stable material for PEDOT:PSS. Thus, we attribute the quicker degradation of the PEDOT:PSS-based device to the more acidic and hygroscopic nature of PEDOT:PSS compared to NiO.

© 2013 WILEY-VCH Verlag GmbH & Co. KGaA, Weinheim

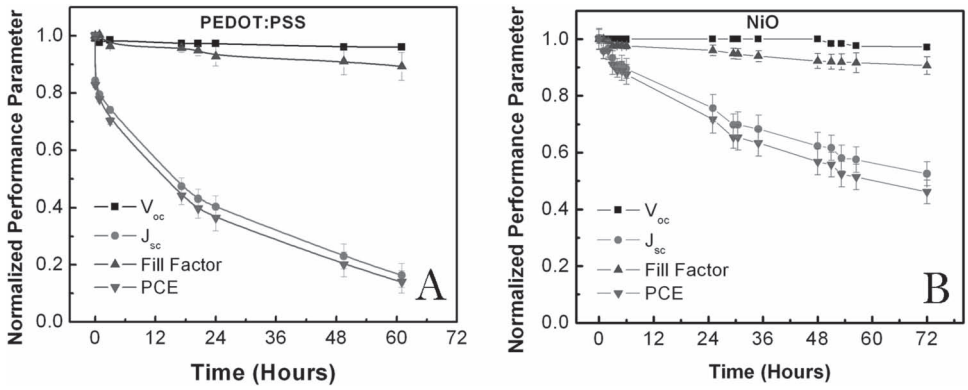

Figure 6. Normalized device characteristics as a function of air exposure time for a) PEDOT:PSS- and b) NiO- based devices. Devices made with NiO HTLs are more stable when stored in ambient conditions, indicating that the NiO HTL is more stable than the PEDOT:PSS HTL in these solar cells.

3. Conclusions

We characterized the physical, chemical, optical, and electronic properties solution-processed NiO and fabricated solar cells using this NiO film as a hole transport layer. We found that ethanol-soluble monoethanolamine coordination complexes of nickel can be thermally decomposed to form NiO. XPS results showed a strong contribution from the Ni^{3+} state, confirming the formation of p-type, non-stoichiometric NiO and the dipolar NiOOH species upon thermolysis of the precursor films. Optical analysis of the NiO thin films showed favorable optical properties for photovoltaic applications. Solar cells incorporating NiO films showed significant enhancements in fill factor and short circuit current, leading to a 14.7% increase in PCE compared with the cells with PEDOT:PSS. The enhancements in the NiO devices were due to improved optical resonance, nanoscale active layer morphology, increased shunt resistance, and lower series resistance for charge extraction in the NiO devices.

4. Experimental Section

NiO Precursor Solution: Nickel acetate tetrahydrate ($Ni(CH_3COO)_2{\cdot}4H_2O$) (Acros Organics) was dissolved in ethanol with monoethanolamine ($NH_2CH_2CH_2OH$) (Sigma-Aldrich) (0.1 mol L^{-1}). The mole ratio of Ni^{2+}: MEA was maintained at 1:1 in solution. Dissolution took place while stirring in a sealed glass vial under air at 70 °C for 4 h. The solution appeared homogeneous and deep green after approximately 40 min.

NiO film preparation: All NiO films were deposited by spin-casting onto the appropriate substrates. For solar cells, the substrates were ITO-coated glass with sheet resistance of 15 ohm sq^{-1}. For GIXRD, the substrates were plain glass. For XPS, the substrates were single crystal Si wafers. All substrates were cleaned by the following procedure before spin-casting: successive sonication in deionized (DI) water, acetone, and isopropyl alcohol baths for 15 min each. Unless otherwise stated, the NiO precursor films were heated to 275 °C for 45 min in air.

Device Fabrication and Characterization: To fabricate the solar cells, ITO-coated glass substrates were UV ozone treated for 15 min between solvent cleaning and spin-casting of the HTL. It was noted, however, that this UV ozone treatment of ITO was not necessary for proper wetting by the NiO precursor solution. PEDOT:PSS (Clevios Al 4083) was filtered through a 0.45 μm PTFE filter prior to spin-casting at 7000 rpm. The PEDOT:PSS films were heated at 140 °C for 10 min in air and transferred immediately to the nitrogen-filled glovebox for further processing. When NiO was used as the HTL instead of PEDOT:PSS, the NiO films were allowed to cool before being transferred to a nitrogen-filled glovebox for further processing. The polymer:fullerene blend ratio is 1:1.5 by weight and is dissolved in chlorobenzene with 5 vol% 1,8-diiodooctane (DIO) additive. $PC_{71}BM$ was acquired from Solenne (purity >99%) and was used as received. The blend was spin-cast on top of the HTL film to give an active layer thickness of 105 nm. The devices were immediately loaded into a thermal evaporator where 1 nm of LiF and 100 nm of Al were deposited under a vacuum pressure of 5×10^{-7} Torr. *J–V* characterization was performed with a Keithley 4200 semiconductor parameter analyzer system with a Newport Thermal Oriel 94021 1000 W solar simulator (4 in. × 4 in. beam size) using the AM1.5 G solar spectrum at 100 mW cm^{-2} incident power. The light intensity was calibrated by an ORIEL 91150V monosilicon reference cell calibrated by Newport Corporation. EQE measurements were conducted using an in-house setup consisting of a Xenon DC arc lamp, an ORIEL 74125 monochromator, a Keithley 428 current amplifier, an SR 540 chopper system and an SR830 DSP lock-in amplifier from SRS. The experimental setup for electroabsorption was described previously.[51]

GIXRD: GIXRD measurements were performed on a Philips XPert MRD with Cu K X-rays (non-monochromatic) with incident angle $\omega = 3°$.

XPS Measurements: XPS data were acquired on a Perkin Elmer 5100 XPS system with a non-monochromatic Al anode X-ray source. Peak deconvolution and analysis was performed in RBD AugerScan version 3.2 software. The adventitious C 1s peak was referenced to 284.8 eV.

Mass Spectrometry Measurements: Solutions were introduced into an Agilent 6210 TOF-MS via direct injection followed by electrospray ionization (ESI) with an autosampler. The mobile phase was spectroscopy grade ethanol from Fisher Scientific and was used as received. Accurate mass identification was performed in MassHunter software.

Supporting Information

Supporting Information is available from the Wiley Online Library or from the author.

Acknowledgements

The authors acknowledge the support of Department of Energy Basic Energy Sciences (Award Number: DE-FG0207ER46464) for the synthesis and characterization of NiO, the Office of Naval Research (Award number: N00014-11-1-0245) for the fabrication and characterization of the solar cells, and the Air Force Office of Scientific Research (Award

© 2013 WILEY-VCH Verlag GmbH & Co. KGaA, Weinheim

number: FA9550-09-1-0320) for the synthesis of the polymers. The authors are grateful to Dr. Valentin Craciun and Eric Lambers of the University of Florida (UF) Major Analytical Instrumentation Center (MAIC) for their expertise in XRD and XPS, respectively, and fruitful discussions. They also thank Romain Stalder for the ionic structure drawing and Mitchell McCarthy and Bo Liu for their assistance with the atomic force microscope. The authors thank the UF Mass Spectrometry facilities in the Department of Chemistry for their expertise and assistance in analysis and to the National Science Foundation for the MS instrumentation.

Received: August 10, 2012
Revised: November 26, 2012
Published online: January 16, 2013

[1] C. E. Small, S. Chen, J. Subbiah, C. M. Amb, S. Tsang, T.-H. Lai, J. R. Reynolds, F. So, *Nat. Photonics* **2011**, *6*, 115.
[2] S. Chen, C. E. Small, C. M. Amb, J. Subbiah, T. Lai, S.-W. Tsang, J. R. Manders, J. R. Reynolds, F. So, *Adv. Energy Mater.* **2012**, *2*, 1333.
[3] M. Jørgensen, K. Norrman, F. C. Krebs, *Sol. Energy Mater. Sol. Cells* **2008**, *92*, 686.
[4] J. J. Berry, N. E. Widjonarko, B. A. Bailey, A. K. Sigdel, D. S. Ginley, D. C. Olson, *IEEE J. Sel. Top. Quantum Electron.* **2010**, *16*, 1649.
[5] R. Betancur, M. Maymó, X. Elias, L. T. Vuong, J. Martorell, *Sol. Energy Mater. Sol. Cells* **2011**, *95*, 735.
[6] J. Kettle, H. Waters, M. Horie, S.-W. Chang, *J. Phys. D: Appl. Phys.* **2012**, *45*, 125102.
[7] D.-C. Lim, Y.-T. Kim, W.-H. Shim, A.-Y. Jang, J.-H. Lim, Y. Do Kim, Y. Jeong, Y. D. Kim, K. H. Lee, *Bull. Korean Chem. Soc.* **2011**, *32*, 1067.
[8] M. S. Ryu, J. Jang, *Sol. Energy Mater. Sol. Cells* **2011**, *95*, 2893.
[9] N. Sun, G. Fang, P. Qin, Q. Zheng, M. Wang, X. Fan, F. Cheng, J. Wan, X. Zhao, *Sol. Energy Mater. Sol. Cells* **2010**, *94*, 2328–2331.
[10] N. Sun, G. Fang, P. Qin, Q. Zheng, M. Wang, X. Fan, F. Cheng, J. Wan, X. Zhao, J. Liu, D. L. Carroll, J. Ye, *J. Phys. D: Appl. Phys.* **2010**, *43*, 445101.
[11] Z. Y. Wang, S.-H. Lee, D.-H. Kim, J.-H. Kim, J.-G. Park, *Sol. Energy Mater. Sol. Cells* **2010**, *94*, 1591.
[12] M. D. Irwin, D. B. Buchholz, A. W. Hains, R. P. H. Chang, T. J. Marks, *Proc. Natl. Acad. Sci. USA* **2008**, *105*, 2783.
[13] E. L. Ratcliff, J. Meyer, K. X. Steirer, N. R. Armstrong, D. Olson, A. Kahn, *Org. Electron.* **2012**, *13*, 744.
[14] K. X. Steirer, J. P. Chesin, N. E. Widjonarko, J. J. Berry, A. Miedaner, D. S. Ginley, D. C. Olson, *Org. Electron.* **2010**, *11*, 1414.
[15] J. G. Aiken, A. G. Jordan, *J. Phys. Chem. Solids* **1968**, *29*, 2153.
[16] D. Adler, J. Feinleib, *Phys. Rev. B* **1970**, *2*, 3112.
[17] S. Hüfner, P. Steiner, I. Sander, F. Reinert, H. Schmitt, M. Neumann, S. Witzel, *Solid State Commun.* **1991**, *80*, 869.
[18] S. Hüfner, J. Osterwalder, T. Riesterer, F. Hulliger, *Solid State Commun.* **1984**, *52*, 793.
[19] H. A. Juybari, M.-M. Bagheri-Mohagheghi, M. Shokooh-Saremi, *J. Alloys Compd.* **2011**, *509*, 2770.
[20] G. A. Sawatzky, J. W. Allen, *Phys. Rev. Lett.* **1984**, *53*, 2339.
[21] K. X. Steirer, P. F. Ndione, N. Edwin Widjonarko, M. T. Lloyd, J. Meyer, E. L. Ratcliff, A. Kahn, N. R. Armstrong, C. J. Curtis, D. S. Ginley, J. J. Berry, D. C. Olson, *Adv. Energy Mater.* **2011**, *1*, 813.
[22] F. A. Kröger, *J. Phys. Chem. Solids* **1968**, *29*, 1889.
[23] S. Mrowec, Z. Grzesik, *J. Phys. Chem. Solids* **2004**, *65*, 1651.
[24] W. K. Chen, N. L. Peterson, *J. Phys. Chem.* **1973**, *34*, 1093.
[25] M. D. Irwin, J. D. Servaites, D. B. Buchholz, B. J. Leever, J. Liu, J. D. Emery, M. Zhang, J. Song, M. F. Durstock, A. J. Freeman, M. J. Bedzyk, M. C. Hersam, R. P. H. Chang, M. A. Ratner, T. J. Marks, *Chem. Mater.* **2011**, *23*, 2218–2226.
[26] C. M. Amb, S. Chen, K. R. Graham, J. Subbiah, C. E. Small, F. So, J. R. Reynolds, *J. Am. Chem. Soc.* **2011**, *133*, 10062.
[27] Y. Park, K. J. Kim, *J. Cryst. Growth* **2003**, *258*, 380.
[28] A. A. Al-Ghamdi, W. E. Mahmoud, S. J. Yaghmour, F. M. Al-Marzouki, *J. Alloys Compd.* **2009**, *486*, 9.
[29] X. Lou, X. Zhao, X. He, *Sol. Energy* **2009**, *83*, 2103.
[30] R. F. Evilia, C. N. Reilley, *J. Coord. Chem.* **1973**, *3*, 7.
[31] K. D. Becker, F. Rau, *Ber. Bunsen-Ges.* **1992**, *96*, 1017.
[32] R. Newman, R. M. Chrenko, *Phys. Rev.* **1959**, *114*, 1507.
[33] S. Uhlenbrock, C. Scharfschwerdt, M. Neumann, G. Illing, H.-J. Freund, *J. Phys. Condens. Matter* **1992**, *4*, 7973.
[34] K. S. Kim, N. Winograd, *Surf. Sci.* **1974**, *43*, 625.
[35] B. Sasi, K. G. Gopchandran, *Nanotechnology* **2007**, *18*, 115613.
[36] M. Tomellini, *J. Chem. Soc., Faraday Trans. 1* **1988**, *84*, 3501.
[37] N. Kitakatsu, V. Maurice, C. Hinnen, P. Marcus, *Surf. Sci.* **1998**, *407*, 36.
[38] B. P. Payne, M. C. Biesinger, N. S. McIntyre, *J. Electron Spectrosc. Relat. Phenom.* **2009**, *175*, 55.
[39] M. A. Langell, C. L. Berrie, M. H. Nassir, K. W. Wulser, *Surf. Sci.* **1994**, *320*, 25.
[40] M. A. Langell, M. H. Nassir, *J. Phys. Chem.* **1995**, *99*, 4162.
[41] E. L. Ratcliff, J. Meyer, K. X. Steirer, A. Garcia, J. J. Berry, D. S. Ginley, D. C. Olson, A. Kahn, N. R. Armstrong, *Chem. Mater.* **2011**, *23*, 4988.
[42] S.-Y. Han, D.-H. Lee, Y.-J. Chang, S.-O. Ryu, T.-J. Lee, C.-H. Chang, *J. Electrochem. Soc.* **2006**, *153*, 382.
[43] A. L. Patterson, *Phys. Rev.* **1939**, *56*, 978.
[44] L. D. Kadam, P. S. Patil, *Sol. Energy Mater. Sol. Cells* **2001**, *69*, 361.
[45] Hereaus Data Sheet, Conducting Polymers Division, Clevios P VP AI 4083, http://clevios.com/media/webmedia_local/media/datenblaetter/81075812_CLEVIOS_P_VP_AI_4083__20101222.pdf **2010**, 81075812 (accessed October 2012).
[46] V. Wood, M. J. Panzer, J. E. Halpert, J.-M. Caruge, M. G. Bawendi, V. Bulovic, *ACS Nano* **2009**, *3*, 3581.
[47] S. Chen, J. R. Manders, S.-W. Tsang, F. So, *J. Mater. Chem.* **2012**, *22*, 24202.
[48] N. E. Widjonarko, E. L. Ratcliff, C. L. Perkins, A. K. Sigdel, A. Zakutayev, P. F. Ndione, D. T. Gillaspie, D. S. Ginley, D. C. Olson, J. J. Berry, *Thin Solid Films* **2012**, *520*, 3813.
[49] S. K. Hau, H.-L. Yip, O. Acton, N. S. Baek, H. Ma, A. K.-Y. Jen, *J. Mater. Chem.* **2008**, *18*, 5113.
[50] S. K. Hau, H.-L. Yip, H. Ma, A. K.-Y. Jen, *Appl. Phys. Lett.* **2008**, *93*, 233304.
[51] P. A. Lane, S. Chen, F. So, *J. Photonics Energy* **2011**, *1*, 011020.
[52] I. Horcas, R. Fernández, J. M. Gómez-Rodríguez, J. Colchero, J. Gómez-Herrero, A. M. Baro, *Rev. Sci. Instrum.* **2007**, *78*, 013705.

© 2013 WILEY-VCH Verlag GmbH & Co. KGaA, Weinheim